ELECTROCHEMISTRY

A zinc-conducting chalcogenide electrolyte

Jian Zhi[1]†, Siwei Zhao[2]†, Min Zhou[3], Ruiqi Wang[2], Fuqiang Huang[1,2]*

A solid-state zinc-ion battery can fundamentally eliminate dendrite formation and hydrogen evolution on the zinc anode from aqueous systems. However, enabling fast zinc ion $^{+}$ conduction in solid crystals is thought to be impossible. Here, we demonstrated a fluorine-doping approach to achieving fast Zn^{2+} transport in mesoporous $Zn_yS_{1-x}F_x$. The substitutional doping of fluoride ion with sulfide substantially reduces Zn^{2+} migration barrier in a crystalline phase, while mesopore channels with bounded dimethylformamide enable nondestructive Zn^{2+} conduction along inner pore surface. This mesoporous conductor features a high room-temperature Zn^{2+} conductivity (0.66 millisiemens per centimeter, compared with 0.01 to 1 millisiemens per centimeter for lithium solid-state electrolyte) with a superior cycling performance (89.5% capacity retention over 5000 cycles) in a solid zinc-ion battery and energy density (0.04 watt-hour per cubic centimeter) in a solid zinc-ion capacitor. The universality of this crystal engineering approach was also verified in other mesoporous zinc chalcogenide materials, which implies various types of potential Zn^{2+}-conducting solid electrolytes.

INTRODUCTION

Because of the increasing demands of sustainable energy applications and the rare nature of Li resources, great efforts have been dedicated to designing energy storage systems beyond Li-ion batteries (LIBs) (*1*). Among them, Zn-ion batteries (ZIBs) and Zn-ion capacitors (ZICs) come out as one of the most economical alternatives due to their advantages of low cost and environmental friendliness (*2*–*4*). However, some safety-related challenges, such as formation of dendrites, corrosion of the zinc anode, and decomposition of electrolyte, are still major obstacles for the practical applications of ZIBs and ZICs.

Constructing solid-state ZIBs and ZICs is a promising strategy for these challenges due to their potential benefits to safety, energy density, and shelf life (*5*). The realization of these energy storage devices largely depends on solid electrolyte based on a Zn superionic conductor. Unfortunately, rare inorganic zinc-conducting solid electrolytes have been reported so far because of the strong electrostatic bonding of Zn^{2+} ions with solid matrix, which results in low room-temperature ionic conductivity (usually less than 10^{-5} S cm^{-1}) along with low Zn^{2+} transference number (generally below 0.4) (*6*). However, Zn^{2+} conduction in these electrolytes largely relies on the addition of free water [15 to 70 weight % (wt %)], which still causes severe surface corrosion and hydrogen evolution on Zn metal. Further seeking of inorganic solid electrolyte with intrinsic high Zn^{2+} conductivity, which shares a similar ion transport mechanism as Li superionic conductors for solid-state LIBs, may be another choice for solid ZIBs and ZICs.

In this work, we report a design strategy for inorganic Zn^{2+} superionic conductors based on facile fluorine doping of mesoporous zinc chalcogenide. This approach was firstly applied in ZnS, a diamond-structured chalcogenide material with tetrahedral coordination geometry. First-principle structure calculations (discussion S1) (*7*, *8*) show that for a large range of Fermi energies, ZnS allows the formation of interstitial Zn^{2+} even with a negative formation energy, indicating that Zn^{2+} interstitials can stably exist in the ZnS matrix (fig. S1). Therefore, ZnS is a promising solid conductor for Zn^{2+} migration, which may create an alternative direction in the development of Zn^{2+}-conducting solid electrolyte.

Here, we present that substitutional doping of F^{-} with S^{2-} introduces abundant Zn vacancies (Vac_{Zn}) in mesoporous ZnS (MZS), which substantially reduce Zn^{2+} migration barrier along adjacent octahedral Zn sites and enable fast Zn^{2+} transport in a crystalline $Zn_yS_{1-x}F_x$ phase. We further show that the mesopore channels of F^{-}-doped MZS (MFZS) with a small amount of bound dimethylformamide [DMF; 6.2 mole percent (mol %)] molecules also assist in nondestructive and rapid Zn^{2+} conduction along the inner pore surface of MFZS. After preinsertion of Zn^{2+}, this ion conductor (Zn-MFZS) shows a high intrinsic ionic conductivity and transference number of 0.66 mS cm^{-1} and 0.76, respectively. Zn-MFZS also presents a wide electrochemical window of −0.5 to 3 V (versus Zn/Zn^{2+}) and realizes hydrogen and dendrite-free Zn plating/stripping (over 1600-hour cycle at room temperature) in a symmetric cell, achieving a record-high cumulative capacity of 4000 mA·hour cm^{-2}.

In addition, Zn-MFZS allows in situ growth of Prussian blue analogs and carbonaceous materials inside mesopores to obtain an active material/solid electrolyte integrated structure. This fundamentally resolves the ion conduction issue for solid thick electrodes and results in a superior electrochemical performance in both solid ZIBs and ZICs. Zn-MFZS also presents many advantages in terms of stability (nonvolatile), safety (nonexplosive), all-climate application (wide temperature window from −40° to 100°C), and scalable potential (low negative/positive electrode capacity ratio (N/P) of 2.41). This fluorine-doping strategy can be used to boost the intrinsic Zn^{2+} conductivity for other mesoporous zinc chalcogenide materials. This leads to a series of high-performance fast ion–conducting Zn^{2+} inorganic conductors that shows great potential in high energy and safe solid-state energy storage systems.

[1]State Key Laboratory of High-Performance Ceramics and Superfine Microstructure, Shanghai Institute of Ceramics, Chinese Academy of Sciences, Shanghai 200050, P. R. China. [2]Beijing National Laboratory for Molecular Sciences and State Key Laboratory of Rare Earth Materials Chemistry and Applications, College of Chemistry and Molecular Engineering, Peking University, Beijing 100871, P. R. China. [3]Hefei National Laboratory for Physical Science at the Microscale, Department of Applied Chemistry, University of Science and Technology of China, Hefei, Anhui 230026, P. R. China.
*Corresponding author. Email: huangfq@mail.sic.ac.cn
†These authors contributed equally to this work.

RESULTS

Structure characterization of MFZS

MFZS was prepared using a facile evaporation-induced self-assembly (EISA) process using Pluronic F127 as a soft template, followed by the calcination at 650°C under argon for the formation of mesostructured ZnS. Fluorine doping was achieved by adding NH_4F aqueous in the sol for EISA (*9*–*11*). As characterized by scanning electron microscopy (SEM) in fig. S2, MFZS shows clusters of rod-like particles with a diameter of 100 to 200 nm. The microstructure of the synthesized MFZS sample with 5.6 atomic % (at %) of fluorine was investigated by transmission electron microscopy (TEM; Fig. 1, A to C). MFZS exhibits a well-ordered mesoporous structure along [100] and [111] direction (Fig. 1, A and B). Attributing to the low association energy between ZnS crystals and hydrophobic F127 chains, this soft-templating method to obtain MZS inevitably leads to the formation of semicrystalline and amorphous phase in the inner wall of MFZS (Fig. 1C). The mesoporous structure of MFZS was further verified by IV-type nitrogen adsorption-desorption isotherm (Fig. 1D), with a pore size centered at 4.58 nm (inset of Fig. 1D) and a high surface area of 257 $m^2 g^{-1}$. The crystal structure of MFZS and pristine MZS was investigated by X-ray diffraction (XRD) spectroscopy. The corresponding peaks are well indexed to cubic sphalerite ZnS without any impurities (JCPDS#05-0566; fig. S3).

X-ray photoelectron spectroscopy (XPS) was further conducted to reveal the chemical state of fluorine dopant in ZnS lattice. As shown in Fig. 1E, the deconvoluted fluorine 1s XPS of MFZS shows two peaks at 686.8 and 685.2 eV, representing the substitutional F^- for S^{2-} and surface absorbed F^-, respectively (*12*). This substitutional doping of mono-ion F^- with divalent ion S^{2-} greatly increases the local positive charges and creates abundant Vac_{Zn} around doping sites to balance the charge distribution, which is evidenced by ^{19}F solid-state magic-angle spinning nuclear magnetic resonance (MAS-NMR; Fig. 1F). Compared to the MAS-NMR of MZS, additional peak appears in the spectra of MFZS at a chemical shift of −173.6 parts per million (ppm), corresponding to the fluorine in the vicinity of Vac_{Zn} (*13*). The introduction of Vac_{Zn} also increases the electronic density around the Zn sites, which leads to a 1.2-eV shift toward lower binding energy in Zn $2p_{1/2}$ and Zn $2p_{3/2}$ peaks for MFZS compared with MZS (Fig. 1G). Rietveld refinement fitting for MFZS was performed by VESTA software using face-centered cubic unit cell for ZnS with

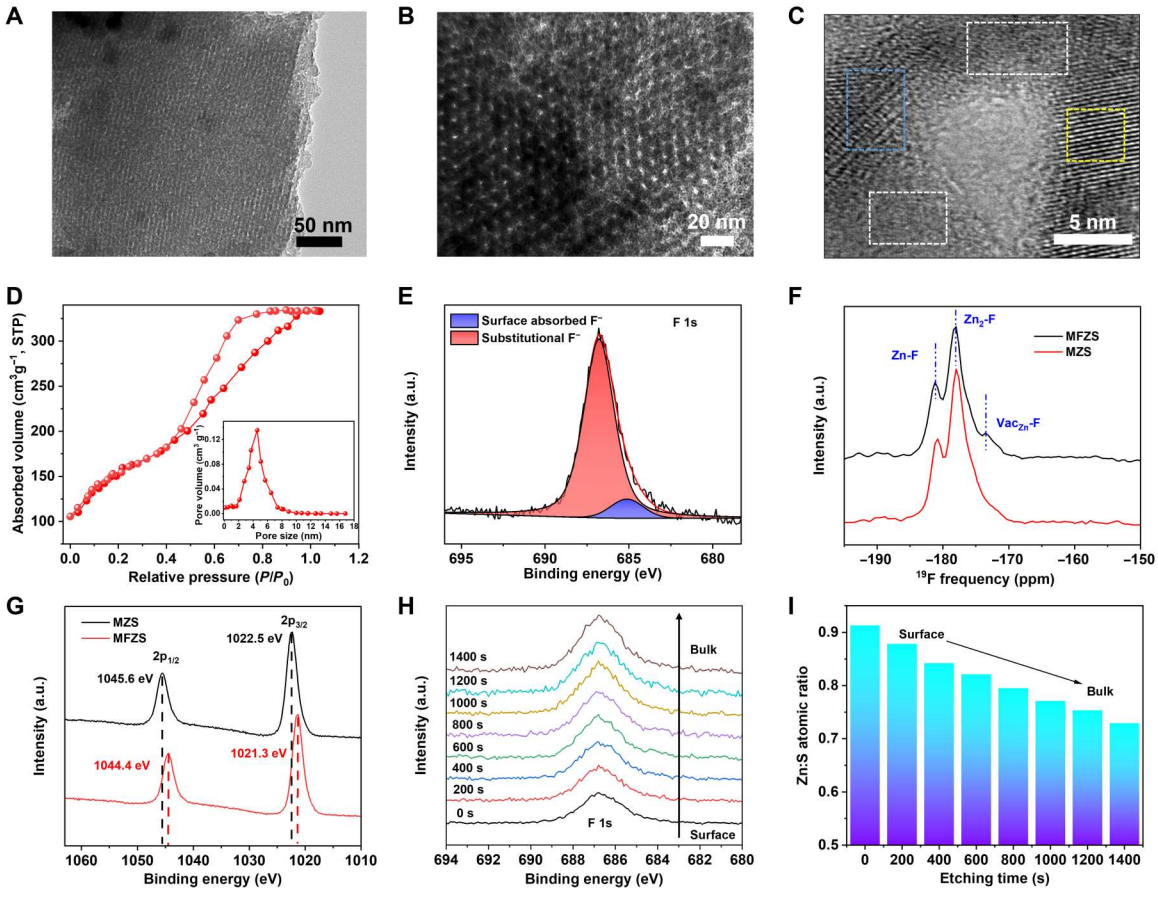

Fig. 1. Characterizations of MFZS. (**A** and **B**) TEM images of MFZS along [100] and [111] direction, respectively. (**C**) High-resolution electron microscopy of MFZS inner wall structure with the combination of crystalline phase (yellow rectangle), semicrystalline phase (blue rectangle), and amorphous phase (white rectangle). (**D**) N_2 adsorption-desorption isotherms and corresponding pore size distribution (inset) of MFZS. (**E**) XPS spectra for F 1s of MFZS. (**F**) MAS-NMR of MFZS and MZS. (**G**) XPS spectra for Zn 2p of MFZS and MZS. (**H**) XPS depth profiles for F 1s of MFZS. (**I**) Zn:S atomic ratio obtained from XPS quantitative analysis along with the Ar^+ etching time. STP, standard temperature and pressure; a.u., arbitrary units.

$\overline{F}43m$ space group (fig. S4). Good agreement between the calculated and observed model was obtained with R_{wp} = 5.98%, R_{exp} = 6.30%, χ^2 = 0.89, and Goodness of Fit (GOF) = 0.94. Table S1 shows the refined structure parameter of MFZS. It is observed that the occupancy ratio of S:F in MFZS is 0.016 (0.015:0.913), suggesting that approximately 1.6% of S sites have been occupied by F^- ions. In addition, the occupancy ratio of Zn:(S + F) in MFZS is only 0.935 (0.868:0.928), further confirming the formation of Vac_{Zn} after fluorine doping. It is also shown that the unit cell volume and crystallite size of MFZS were smaller than those of pristine MZS (table S2), indicating an obvious lattice shrinkage. This is in accordance with Vegard's rule in a lattice parameter reduction due to the replacing of larger S^{2-} ions with smaller F^- ions (*14*).

Ar^+ sputtering-assisted XPS was measured on MFZS samples to get better fluorine-doping statistics from the surface to the bulk. As the etching time increased, a steady increase in F 1s signals can be clearly seen in Fig. 1H. It is due to the well-ordered mesopore channels (Fig. 1A) and amorphous wall structure (Fig. 1C), which greatly promote the penetration of F^- during calcination and lead to the introduction of abundant Vac_{Zn} into the bulk crystals of ZnS. This bulk Vac_{Zn} is also verified by the decrease in Zn:S atomic ratio as a function of etching time in XPS quantitative analysis (Fig. 1I). Last, we emphasize that fluorine-doping concentration can be continuously adjusted by changing NH_4F concentration in EISA sol (fig. S5).

Zn conduction in Zn-MFZS

To introduce more mobile Zn^{2+} for ionic conduction, MFZS was mixed with a zinc salt solution {0.5 M zinc trifluoromethanesulfonate [$Zn(OTF)_2$] in DMF}, followed by evaporation of DMF to obtain Zn-MFZS conductor [the molar ratio of $Zn(OTF)_2$ to MFZS is about 1:10]. Zn-MFZS contains a small amount of bound DMF (6.2 mol %) as determined from ultrasonic extraction–based gas chromatography–mass spectrometry (GC-MS) method, which shows a molecular formula of $Zn_yS_{1-x}F_x(CF_3SO_3)_z{\cdot}0.066$ DMF. Compared to the differential scanning calorimetry (DSC) curve of liquid DMF, Zn-MFZS does not show a phase change near −69.2°C (fig. S6), indicating that the DMF are isolated (gas-like dimers) in two-dimensional nanochannels of MFZS and does not form a liquid phase (*15*). Fourier transform infrared spectra of Zn-MFZS also show a decreased peak intensity at 1257 cm^{-1} in C═N stretching, further suggesting the weak DMF-DMF interaction in Zn-MFZS (fig. S7) (*16*, *17*). Obviously, DMF molecules do not agglomerate into a condensed liquid phase in Zn-MFZS and therefore do not function as a solvent in this system. This is substantially different from the electrolytes with free liquid solvent, in which the solvent molecules exist as bulk liquid and directly enable ionic conduction. Zn-MFZS shows high electrochemical stability with a wide potential range from −0.5 to 3 V, whereas the oxygen evolution for aqueous electrolyte (2 M $ZnSO_4$) begins at 1.8 V (Fig. 2A). Zn-MFZS is also an excellent Zn^{2+} conductor. At 25°C, Zn-MFZS presents a high Zn^{2+} conductivity of 0.66 mS cm^{-1} (fig. S8) with a high transference number of 0.76 (discussion S2) (*18*, *19*), which is much higher than that of pristine MZS (0.025 mS cm^{-1}), MFZS (0.18 mS cm^{-1}), Zn^{2+} preinserted MZS (Zn-MZS, 0.027 mS cm^{-1}; fig. S9), and other solid or hybrid Zn^{2+} conductors (Fig. 2B) (*6*, *20*–*22*). The conductivity-temperature relationship of Zn-MFZS follows an Arrhenius-type behavior (Fig. 2C), and the activation energy of Zn-MFZS was calculated to be 0.3 eV (fig. S10). Moreover, Zn-MFZS also exhibits extremely low electronic conductivity of about 6.1×10^{-7} mS cm^{-1} at 25° to 300°C (fig. S11). The high electronic conductivities of Zn^{2+}-conducting solid electrolyte allow Zn^{2+} to combine with electrons to form Zn dendrites in the electrolytes after the potential reaches the Zn-plating potential. The dendrites nucleation inside the solid electrolyte could further boost the electronic conductivity, which would facilitate the Zn dendrite deposition until a metallic percolation is formed and lead to short circuiting. Similar phenomena were reported in sodium solid electrolytes, where the enhanced electronic conduction in sodium β-alumina can result in sodium deposition in the electrolyte (*23*, *24*). The low electronic conductivity and high ionic conductivity of Zn-MFZS suggest its promising application in dendrite-free all-solid-state ZIBs. We also found that 5.6 at % of fluorine doping is critical in the ionic conductivity of Zn-MFZS. Further increase in the doping concentration to 6.2 at % inevitably increases the surface adsorbed F^- and decreases the substitutional F^- (table S3), which leads to a notable reduction in ionic conductivity (fig. S12).

To exclude the impact of DMF on Zn^{2+} conduction of Zn-MFZS, we used spark plasma sintering (SPS) to study the intrinsic Zn^{2+} conduction in MFZS solid crystals (fig. S13). After SPS, the obtained sample (Zn-$MFZS^{SPS}$) still shows a mesoporous structure (fig. S14) without any detectable DMF from gas chromatography–mass spectrometry (GC-MS). The conductivity-temperature relationship of Zn-$MFZS^{SPS}$ also follows the Arrhenius equation (Fig. 2C) with a Zn^{2+} conductivity of 0.43 mS cm^{-1} at room temperature (Fig. 2D), which is still 65% to the value of Zn-MFZS (0.66 mS cm^{-1}). The ionic conduction of Zn-MFZS is mainly derived from the Zn^{2+} migration in the bulk solid phase, and Zn-MFZS is absolutely a solid electrolyte. The Zn^{2+} conductivity of this DMF-free Zn-$MFZS^{SPS}$ is still much larger than those of previously reported Zn^{2+} inorganic conductors, including MOF-808 (0.21 mS cm^{-1}) (*20*), ZIF-8 (0.019 mS cm^{-1}) (*21*), zinc silicate (0.028 mS cm^{-1}) (*6*), and $Bi_2Zn_{0.1}V_{0.9}O_{5.35}$ (0.034 mS cm^{-1}) (*22*) featuring an outstanding solid-state Zn^{2+} conductor. Similar trend can be also observed between Zn-MZS and SPS-treated Zn-MZS samples (Zn-MZS^{SPS}; Fig. 2D), indicating that the bound DMF molecules in mesopore channels also contribute to the high ionic conductivity of Zn-MFZS. To understand the role of residue DMF in Zn-MFZS for Zn^{2+} transport, we performed molecular dynamics (MD; discussion S3) (*25*) simulations for fluorine-doped ZnS systems with different numbers of DMF molecules and $Zn(OTF)_2$ salts. Compared to the systems with 110 OTF^- ions, the addition of 75 DMF molecules leads to a much larger mean squared displacement of Zn^{2+} ions (Fig. 2E) and substantially higher Zn^{2+} diffusion coefficient (from 0.47×10^{-7} to 1.1×10^{-7} cm s^{-1}; table S4). This is due to the much faster movement of DMF molecules than OTF^- ions in fluorine-doped ZnS (fig. S15), which taps Zn^{2+} out of its bonding sites with OTF^- and effectively assist Zn^{2+} interfacial transport in the inner pore surface of Zn-MFZS. Note that on the basis of MD simulations (fig. S15), the counteranion OTF^- shows a high diffusion coefficient of 1.22×10^{-7} cm^2 s^{-1} that is even comparable to the value of Zn^{2+} (table S4). OTF^- anion also contributes to the ionic conductivity of the solid electrolyte, and Zn-MFZS is a typical dual-ion conductor. Nevertheless, the actual migration of OTF^- is largely trapped by the electrophilic fluorine atoms in MFZS matrix (*26*), which accounts for the much lower transference number

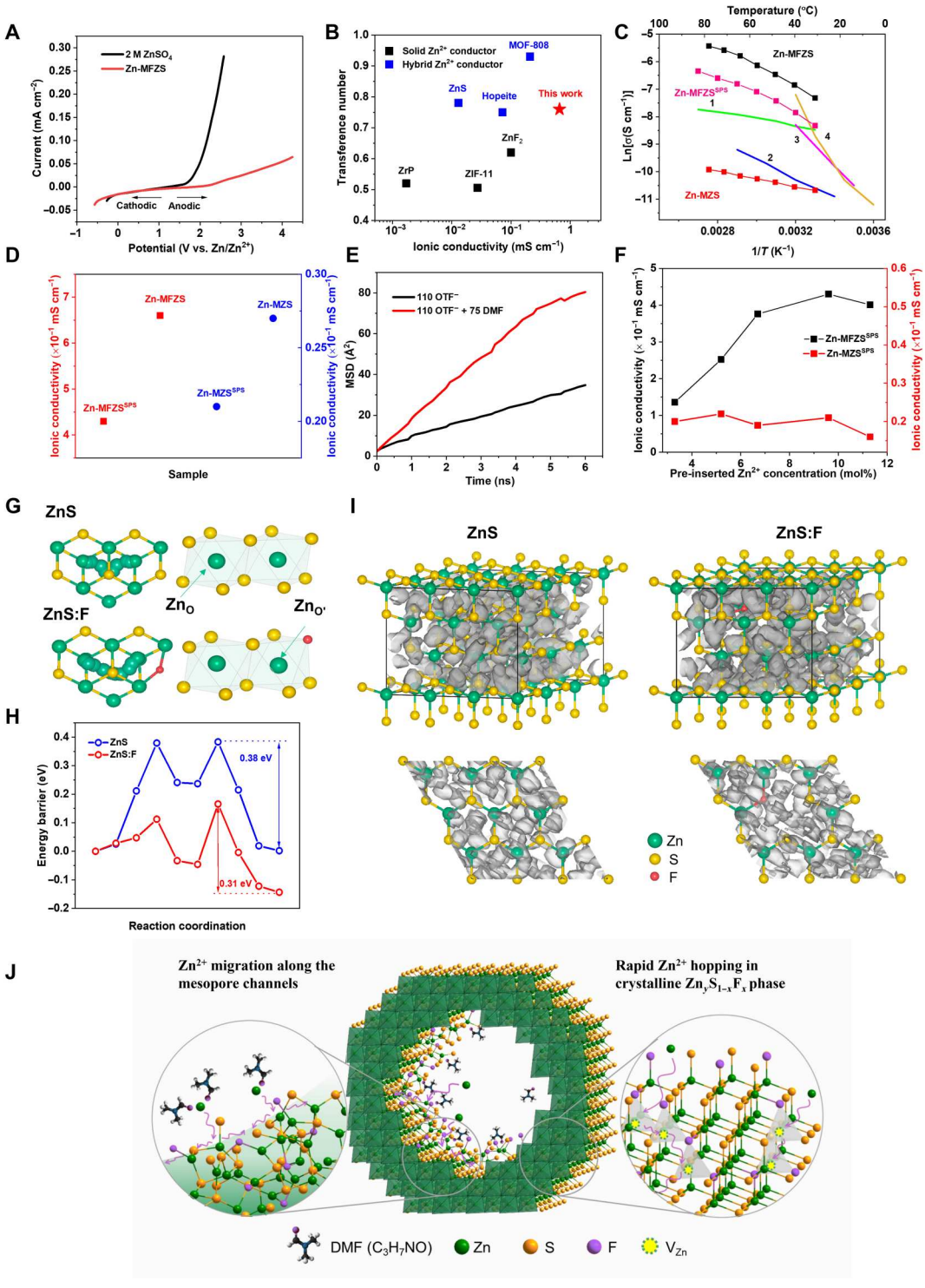

Fig. 2. Zn conduction in Zn-MFZS. (**A**) Linear sweep voltammetry (LSV) of Zn-MFZS under 0.1 mV s^{-1} [anodic scan, open-circuit voltage (OCV) to 4.2 V; cathodic scan, OCV to −0.57 V]. The LSV of 2 M $ZnSO_4$ aqueous electrolyte was also measured for comparison. (**B**) Transference number and ionic conductivity for Zn-MFZS and other inorganic solid Zn^{2+} conductors with (blue) or without liquid solvent (black) including MOF-808 (*20*), hopeite (*62*), ZnS (*64*), ZnF_2 (*65*), ZrP (*66*) (the transference number is missing from ZnF_2 and ZrP, we prepared the same materials via the same procedures as in (*65*) and (*66*) to obtained these data), and ZIF-11 (*67*). (**C**) Temperature-dependent conductivity of Zn-MFZS, Zn-$MFZS^{SPS}$, and Zn-MZS with linear fitting based on the Arrhenius equation. Temperature-dependent conductivity plots (1 to 4) for previously reported solid Zn^{2+} conductors are also included for comparison, such as MOF-808 (1) (*20*), ionic liquid incorporated ZIF-8 (2) (*21*), zinc silicate (3) (*6*), and $Bi_2Zn_{0.1}V_{0.9}O_{5.35}$ (4) (*22*). (**D**) Ionic conductivities of Zn-MFZS, Zn-$MFZS^{SPS}$, Zn-MZS, and Zn-MZS^{SPS}. (**E**) Mean squared displacement (MSD) of Zn^{2+} in fluorine-doped ZnS systems with 110 OTF^- ions and 110 OTF^- ions + 75 DMF molecules. (**F**) Ionic conductivities of Zn-$MFZS^{SPS}$ and Zn-MFZS samples with different preinserted Zn^{2+} concentrations. (**G** and **H**) Diffusion path (G) and energy profile comparison (H) of Zn^{2+} in ZnS and F-doped ZnS (ZnS:F) along adjacent octahedral Zn sites. (**I**) The probability densities of Zn-ion diffusion in ZnS (left) and ZnS:F (right). (**J**) Schematic illustration of Zn^{2+} conduction in Zn-MFZS electrolyte.

(0.24) than Zn^{2+} (0.76). Similar ionic conduction mechanism has also been reported for a Mg^{2+} conductor MIL-101 ⊃ $[Mg(TFSI)_2]_{1.6}$, in which the mobile carriers are mainly derived from the Mg(II) bis(trifluoromethanesulfonyl)imide $[Mg(TFSI)_2]$ salt and the transport number of Mg^{2+} is 0.41 (*27*).

To study the impact of the introduced $Zn(OTF)_2$ on the ionic conduction of Zn-MFZS crystals, we prepared a series of Zn-$MFZS^{SPS}$ samples with different preinserted Zn^{2+} concentrations. The room-temperature ionic conductivity of Zn-$MFZS^{SPS}$ increases with the increase in preinserted Zn^{2+} concentration and achieves a highest value of 0.43 mS cm^{-1} at a $Zn(OTF)_2$ content of 9.6 mol % (Fig. 2F). It is 2.56 times higher than the ionic conductivity of the SPS-treated MFZS (MFZS^{SPS}; 0.12 mS cm^{-1}) under the same fluorine-doping concentration (5.6 at %; fig. S16). Obviously, the

impregnated $Zn(OTF)_2$ introduced abundant Zn^{2+} carriers and substantially boost the ionic conductivity of Zn-MFZS. In sharp contrast, there are no obvious changes in ionic conductivities from Zn-MZS^{SPS} samples with different preinserted Zn^{2+} concentrations (Fig. 2E), indicting the extremely slow Zn^{2+} diffusion kinetics in pristine ZnS samples. We further found that the ionic conductivity of $MFZS^{SPS}$ without additional Zn^{2+} insertion ($MFZS^{SPS}$) can be adjusted by varying the fluorine-doping concentration (Fig. 2F). Therefore, we conclude that the high Zn^{2+} conductivity of Zn-$MFZS^{SPS}$ is mainly due to the hoping of Zn^{2+} from $Zn(OTF)_2$, while some Zn^{2+} from original MFZS can also move and contribute to the Zn^{2+} conduction. We also prepared a series of nonmesoporous fluorine-doped ZnS particles to study the function of mesopore channels in ionic conduction of Zn^{2+}. With similar ranges of fluorine-doping concentration, SPS-treated fluorine-doped ZnS particles (FZS^{SPS}) show a much lower ionic conductivity than $MFZS^{SPS}$ samples (fig. S17). Obviously, the abundant mesopore channels in MFZS provide more free space for Zn^{2+} migration, which forms continuous, nondestructive Zn^{2+} conduction pathways and notably enhances Zn^{2+} transfer kinetics.

The defect chemistry of fluorine-doped ZnS plays a key role to enable fast Zn^{2+} conduction in MFZS bulk crystals. During F doping, the aliovalent anion substitution occurs in the ZnS lattice, which generates substitutional anion defects and companionable cation vacancy defects. S is eventually replaced by F, which refers to substitutional defects (F_S). The substitution of monovalent F to divalent S would change the overall charge within ZnS. To maintain the electrical neutrality of the compound, the charge compensation is required. Therefore, Vac_{Zn} are formed to balance the charge distribution. The aliovalent anion substitution would not only change the lattice structure due to variant dopant sizes but also influence the electronic structure by tuning electron densities around anions and vacancies (*28*).

The theoretical calculations further reflect the synergic effects of F_S and Vac_{Zn} on MFZS samples from the following aspects. (i) Lattice parameters. A fluoride-doped ZnS model with Vac_{Zn} (labeled as ZnS:F) was established and geometrically optimized as shown in fig. S18 and table S5. The F atom is doped on the original (111) plane of cubic ZnS, which is the (100) plane of the ZnS:F cell. Considering smaller ion radii and stronger zincophilicity of F, the F_S is off-center ions that deviate from the original equilibrium position of S. The smaller F and more vacant surrounding vicinity could trigger lattice reduction, which is in accordance with the shortened supercell axes as observed after F doping in table S5. (ii) Electronic structure. The electronic structure of ZnS and defect-introduced derivatives is analyzed according to the profiles of the density of states in fig. S19. The pristine ZnS is innately a band insulator, where the valence electrons of Zn are transferred to S. Hence, the projected S orbitals dominate the valence band maximum (VBM; fig. S19A). By introducing F_S defects without cation vacancies, the compound is electrically positive because of the smaller oxidant states of F. To balance the charge, the electron filling is increased, where the conduction bands are leveled down to the Fermi level (fig. S19B). By introducing Vac_{Zn}, the electron charge densities around anions would intensify, which is elucidated by the strengthened VBM around Fermi level (fig. S19C). With the cointroduction of F_S and Vac_{Zn}, the positive charge originated from aliovalent anion substitution is compensated by cation vacancies, and the conduction band minimum levels off as pristine ZnS (fig. S19D). (iii) Zn^{2+} diffusion barriers and probability densities. The diffusion behavior of Zn^{2+} is regulated by F doping both energetically and kinetically. Figure 2G shows the Zn^{2+} diffusion profile between octahedral site (Zn_O) and corner-shared tetrahedral S-coordinated sites (Zn_T). Although the most energetically favorable Zn^{2+} transport path between adjacent Zn_T exhibits a barrier of 0.27 eV, the overall Zn^{2+} diffusion performance is lagged by the high-energy Zn_O transfer (0.38 eV; Fig. 2H). When replacing one S atom by F, the energy barrier along adjacent octahedral Zn sites ($Zn_{O'}$) is decreased to 0.31 eV (Fig. 2H), which contributed to the more flexible ZnS lattice after the introduction of F_S and Vac_{Zn}. The Ab Initio Molecular Dynamics (AIMD) simulation visualizes the Zn^{2+} probability densities in Fig. 2I. Because of the zincophilicity of F_S and alleviated the steric effect of Vac_{Zn}, the Zn^{2+} channels become more intense specifically near the defective areas, which shows enhanced Zn^{2+} conductivity (fig. S20). Overall, F doping introduces both F_S and Vac_{Zn}, which facilitates energetically favorable and rapid Zn^{2+} transport in the ZnS lattice.

To sum up, the preinserted $Zn(OTF)_2$ salt provides sufficient Zn^{2+} mobile carriers for ion conduction in Zn-MFZS electrolyte, and the high ionic conductivity of Zn-MFZS is mainly derived from the following two aspects:

1) Fast and nondestructive Zn^{2+} migration along the mesopore channels of Zn-MFZS. The amorphous $Zn_yS_{1-x}F_x$ from the mesopore walls introduces locally disordered structures to enable the lower percolation energy barrier and reduce the friction between Zn^{2+} and mesopore walls (*29*, *30*), while the residue DMF molecules in the pores knocked Zn^{2+} out of the trapping sites and further boost Zn^{2+} conduction (Fig. 2J, left circle).

2) Rapid Zn^{2+} hopping in a crystalline $Zn_yS_{1-x}F_x$ phase. It is realized by the introduction of Vac_{Zn} by substitutional doping of F^- with S^{2-}, which leads to more flexible ZnS lattice and reduced Zn^{2+} migration barrier along adjacent octahedral Zn sites (Fig. 2J, right circle).

Zn anode stability with zinc chalcogenide electrolyte

The impact of Zn-MFZS solid electrolyte on the electrochemical stability of Zn anode was firstly examined by galvanostatic cycling of Zn/Zn-MFZS/Zn symmetric cell (Fig. 3A, with enlarged details in fig. S21). At high current density (5 mA cm^{-2}) and large per-cycle areal capacity (15 mA·hour cm^{-2}), the symmetric cell with Zn-MFZS presents stable voltage profile over 1600 hours for a cumulative plating capacity of 4000 mA·hour cm^{-2} with an overpotential of 36 mV. It is, to the best of our knowledge, the highest cumulative capacity for Li (hollow circle) and Zn anodes (filled circle; Fig. 3B). In contrast, symmetric cell with aqueous electrolyte (2 M $ZnSO_4$) shows an irregularly fluctuating voltage and failed after 400 hours, attributing to the accumulation of Zn dendrites. The electrochemical impedance spectroscopy (EIS) of symmetrical cells with Zn-MFZS electrolyte and aqueous electrolyte was also carried out along with the cycling tests. As shown in fig. S22, the semicircle at high-to-medium frequencies was assigned to the interfacial charge transfer resistance (R_{ct}), whereas the real axis intercept is the equivalent series resistance (R_s). After fitting by the relevant equivalent circuit model (fig. S23 and table S6), the cell with Zn-MFZS exhibits less reduction of R_{ct} (from 247 to 226 ohms; fig. S22) after 500 hours of cycling in comparison to the value (from 154 to 47 ohms) in symmetric cell with aqueous electrolyte, further confirming the stable Zn growth under mesoporous solid

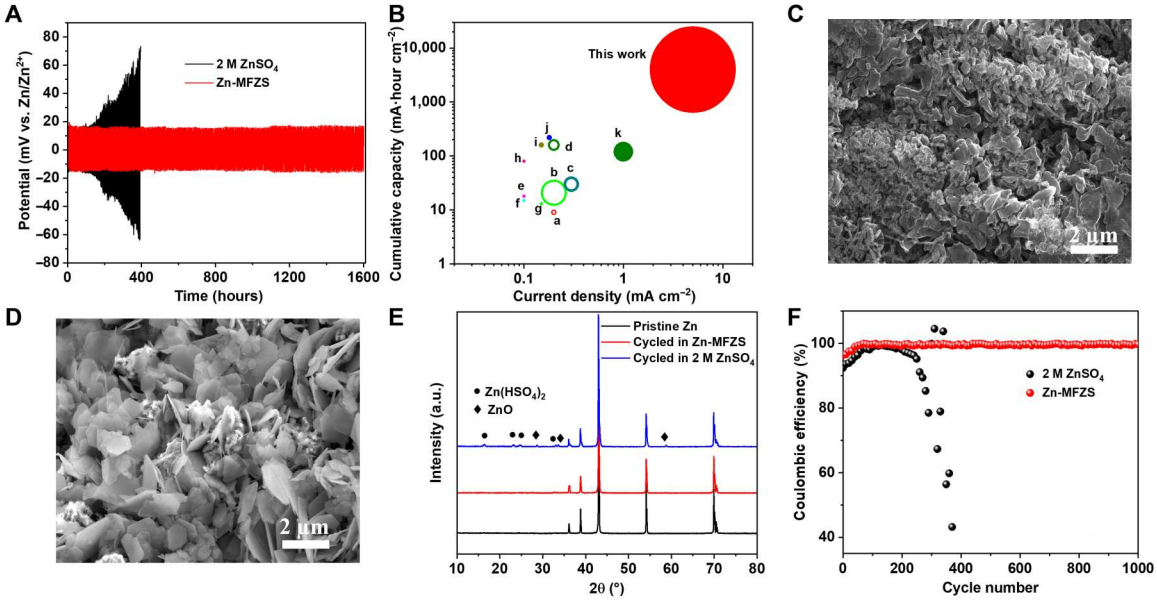

Fig. 3. Long-term stability of Zn anode. (**A**) Zn plating/stripping performance of Zn/Zn symmetric cell with 2 M $ZnSO_4$ and Zn-MFZS under a current density of 5 mA cm^{-2} at room temperature. (**B**) Comparison of cumulative capacity and per-cycle areal capacity (size of each circle) versus current densities between Zn/Zn-MFZS/Zn cell in this work and previous reports at room temperature. Points and references include the following: a (*68*), b (*69*), c (*70*), d (*71*), e (*72*), f (*72*), g (*73*), h (*74*), i (*75*), j (*76*), and k (*77*). Hollow circle, symmetric cells with Li anode; filled circle, symmetric cells with Zn anode. (**C** and **D**) SEM images of Zn anode in symmetric cell with Zn-MFZS (C) and 2 M $ZnSO_4$ (D) aqueous electrolyte after long-term cycling for 1000 hours at 1 mA cm^{-2}. (**E**) XRD patterns of pristine Zn anode before plating/stripping cycles and Zn anode from the cell with 2 M $ZnSO_4$ and MFZS after 1000 hours of cycling at 1 mA cm^2. (**F**) Coulombic efficiency of Zn plating/stripping in symmetric cell with 2 M $ZnSO_4$ and Zn-MFZS at 1 mA cm^{-2}.

electrolyte. The corrosion properties of aqueous and Zn-MFZS solid electrodes were analyzed by linear polarization experiments (fig. S24). The Zn/Zn symmetrical cell with Zn-MFZS showed a lower corrosion current of 0.933 mA cm^{-2} compared with 2.197 mA cm^{-2} of 2 M $ZnSO_4$. Zn-MFZS–based symmetrical cell also exhibits a higher corrosion potential (about 60 mV) than an aqueous cell. These results strongly indicate that Zn-MFZS solid electrolyte can effectively protect Zn from corrosion during storage, which is crucial to suppress hydrogen evolution reaction at the surface of Zn anode (*31*, *32*).

The morphology changes in Zn anode during cycling also provide solid evidence for the protection mechanism of Zn-MFZS electrolyte. SEM images of Zn anode from Zn/Zn-MFZS/Zn cell presenta compact surface (Fig. 3C) without any dendrites and ZnO impurities (Fig. 3E) after 1000 hours of cycling at 1 mA cm^{-2}. In contrast, the Zn anode from the cell with aqueous electrolyte displays massive amounts of dendritic Zn (Fig. 3D) with insulated $Zn(HSO_4)_2$ and ZnO (Fig. 3E). Even at a high rate of 10 mA cm^{-2} with a per-cycle areal capacity (10 mA·hour cm^{-2}), the Zn/Zn- MFZS/Zn symmetric cell can still be operated steadily for 350 hours with an overpotential of 79 mV (fig. S25). Under this high current, the Zn anode also shows a relatively clean surface without any sharp and Zn dendrite flakes (fig. S26), further suggesting the uniform electrochemical plating/stripping of Zn during repeated cycling.

On the basis of the ratio of charge passed in each component, the Coulombic efficiency of Zn/Zn-MFZS/Zn cell reaches 99% within only 50 cycles and retains for 1000 cycles (Fig. 3F). In comparison, the cell with aqueous electrolyte shows much lower Coulombic efficiency and quickly fails after 250 cycles (Fig. 3F). Furthermore, the H_2 evolution during Zn plating/stripping is in situ monitored in a cell–GC-MS instrument. Per-cycle H_2 (0.0627 μmol cm^{-2}) is detected from the symmetric cell with aqueous electrolyte (fig. S27), which is due to the increased contact between electrolyte and Zn anode with uneven Zn deposition. The H_2 evolved in the rest process (0-cycle, 4.6 μmol cm^{-2}) is derived from chemical oxidation of aqueous solution. In sharp contrast, there was almost no H_2-detected Zn/Zn-MFZS/Zn cell (fig. S27).

Electrochemical characterization of solid ZIBs and ZICs with zinc chalcogenide electrolyte

The highly porous feature of Zn-MFZS enables us to develop an integrated cathode material-solid electrolyte structure to overcome the excessive contact impedance in solid batteries. As shown in Fig. 4A, the in situ grown manganese hexacyanoferrate (MnHCF) is randomly located inside or even outside the mesoporous Zn-MFZS with the MnHCF content of roughly 75 wt % (Fig. 4A). The XPS survey spectrum (fig. S28) also shows the intergrowth of MnHCF on Zn-MFZS matrix. The mesopore channels of Zn-MFZS cannot limit the growth of MnHCF, and there is no bottleneck for the integrated amount of MnHCF on Zn-MFZS matrix. The incorporated Zn-MFZS forms an ion-percolation network in the cathode, which shows a high ionic conductivity of 0.13 mS cm^{-1} with a MnHCF content of 75 wt % (fig. S29). However, further increase in the mass ratio of MnHCF beyond 75 wt % leads to the notable reduction in the ionic conductivity (fig. S29). It is possibly due to the agglomeration of MnHCF particles inside and outside of Zn-MFZS channels, which blocks the ion diffusion pathways and inhibits the ionic percolation. With this integrated cathode material (MnHCF@Zn-MFZS), the assembled solid ZIB using Zn-MFZS as

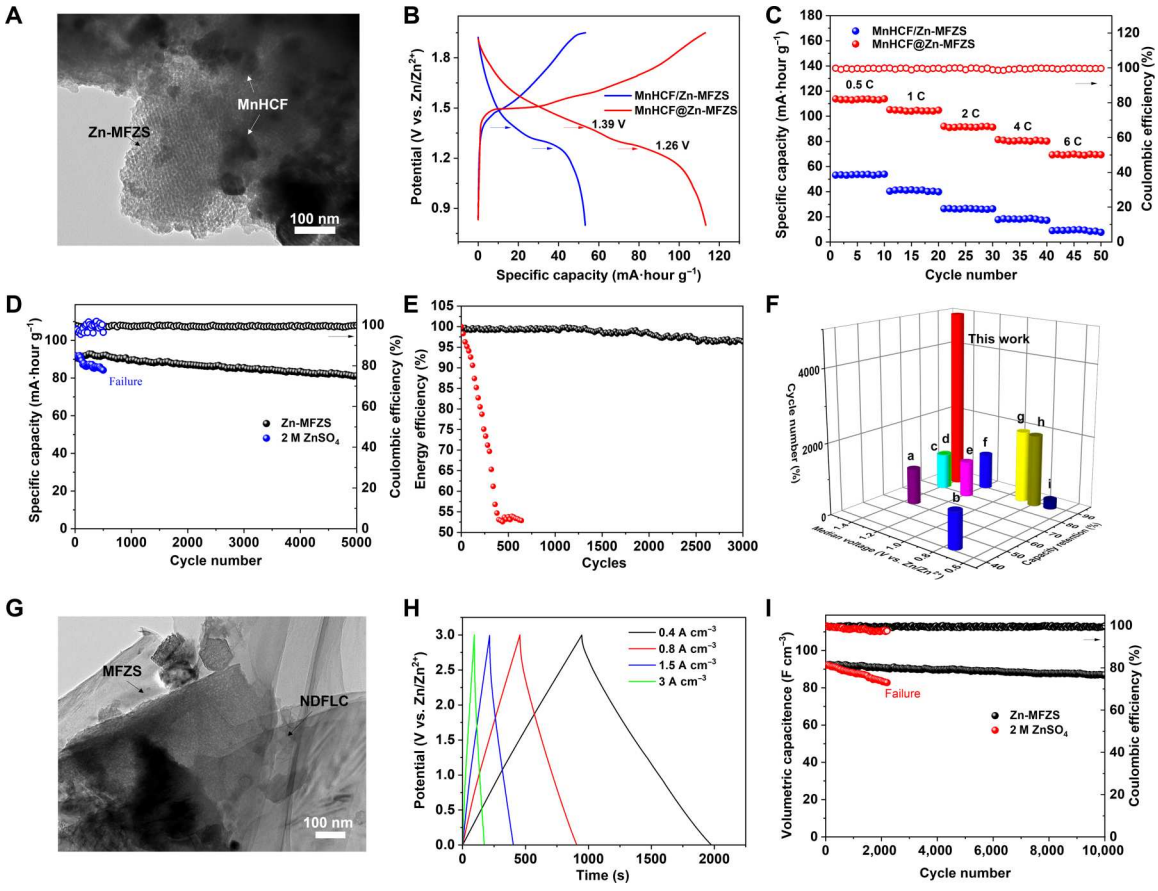

Fig. 4. Electrochemical performance of solid-state full cells and capacitors. (**A**) High-resolution TEM (HR-TEM) of MnHCF in situ grown on Zn-MFZS. MnHCF particles are either inside the mesopores or on the surface of Zn-MFZS. (**B**) Galvanostatic charge/discharge (GCD) curves of solid ZIBs using nonintegrated (MnHCF/Zn-MFZS) and integrated (MnHCF@Zn-MFZS) cathode material. The mass ratio of Zn-MFZS in the composite is roughly 20 wt %. (**C**) The rate performance of MnHCF@Zn-MFZS– and MnHCF/Zn-MFZS–based solid ZIBs. (**D**) Cycling stability of MnHCF-based ZIBs with Zn-MFZS (using MnHCF@Zn-MFZS integrated cathode material) and aqueous $ZnSO_4$ electrolyte at 2 C. (**E**) Energy efficiency of MnHCF-based ZIBs with Zn-MFZS (using MnHCF@Zn-MFZS integrated cathode material) and aqueous $ZnSO_4$ electrolyte. (**F**) Contrast of cycling stability between MnHCF@Zn-MFZS–based solid ZIBs and other reported quasi–solid-state ZIBs: a (*78*), b (*79*), c (*80*), d (*81*), e (*82*), f (*83*), g (*84*), h (*85*), and i (*20*). (**G**) HR-TEM of nitrogen-doped few-layer carbon (NDFLC) in situ grown on Zn-MFZS, which reveals a graphite-like sheets stacked on Zn-MFZS. (**H**) GCD curves of solid ZIC with NDFLC@Zn-MFZS integrated electrode material at different current densities. (**I**) Cycling stability of ZIC with Zn-MFZS (using NDFLC@Zn-MFZS integrated electrode material) and aqueous $ZnSO_4$ electrolyte.

solid electrolyte and Zn metal as anode displays two gentle slopes around 1.39 and 1.26 V in the discharge curves (Fig. 4B), which corresponds to the redox reaction of MnHCF [Mn(III) to Mn(II) and Fe(III) to Fe(II)], respectively.

Note that because of the small mesopore size (4.58 nm), the actual amount of MnHCF grown in the mesopore channels of MFZS could be quite low. However, in situ interfacial growth of MnHCF on MFZS matrix can form intimate solid-solid contact due to strong interfacial binding, thus constructing 3D Zn^{2+} transport pathways in these integrated cathode composites. As shown in fig. S30, the integrated MnHCF@Zn-MFZS shows a percolation threshold of 12.3 volume % to form an ionic conductive network, corresponding to 5.7 wt % of the Zn-MFZS in the composite. In sharp comparison, the nonintegrated MnHCF/Zn-MFZS prepared via physically mixing shows a much higher ionic percolation threshold (26 volume %), indicating a sluggish Zn^{2+} diffusion kinetics. Attributing to the formation of a continuous ion-conducting network, solid ZIB with this integrated MnHCF@Zn-MFZS with a mass loading of 5 mg cm^{-2} shows a specific capacity of 113 mA·hour g^{-1} at 0.5 C (Fig. 4B), which is two times larger than that (53 mA·hour g^{-1}) in solid ZIB with nonintegrated MnHCF/Zn-MFZS cathode. In addition, MnHCF@Zn-MFZS–based solid ZIB also shows a superior rate capability than solid ZIB with nonintegrated cathode (Fig. 4C). These results strongly demonstrate the promising potential of integrated MnHCF@Zn-MFZS cathode in the development of high-performance solid ZIBs.

This solid ZIB also exhibits a stable cycling at 2 C with 89.5% capacity retention over 5000 cycles and high Coulombic efficiency (~99%; Fig. 4D) and high energy efficiency (~96.3%; Fig. 4E). This performance matric is superior to MnHCF-based ZIBs with aqueous 2 M $ZnSO_4$ electrolyte that rapidly falls after 500 cycles (Fig. 4D) and outperforms all reported quasi–solid-state ZIBs (Fig. 4F). It is well known that the cycling performance of aqueous battery strongly depends on the experimental conduction. To make a fair comparison for the cycling data between different battery systems, the authors performed the cycling test of solid

ZIB at 1 A g^{-1} (roughly 6 C; fig. S31). Such a high rate is more frequently used in the evaluation of cycling life for aqueous batteries (*33*, *34*). As shown in fig. S31, the solid ZIB with Zn-MFZS electrolyte shows a capacity retention of 96.4% over 2000 cycles, which is superior to the cycling performance of state-of-the-art optimized aqueous ZIBs under the same rate (fig. S32) (*33*–*41*). Figure S33 shows the EIS spectra for the full cells with Zn-MFZS and aqueous electrolyte. After fitting the Nyquist plot through equivalent circuit in fig. S23, the R_{ct} of ZIB with aqueous electrolyte increases from 306.71 ohms before cycling to 843.51 ohms after 100 cycles at 1 C, which is due to the emergence of by-products [$(Zn_4SO_4(OH)_6{\cdot}5H_2O$] on the electrode surface after cycling. Encouragingly, the R_{ct} of ZIB with Zn-MFZS only increases from 412.61 to 567.83 ohms, indicating a stable electrode/electrolyte interface during cycling.

To determine the role of DMF in the stabilization of cathode/electrolyte interface, we also fabricated a quasi-solid ZIB using nonmesoporous fluorine-doped ZnS as electrolyte (Zn-FZS) and MnHCF@Zn-FZS as cathode, with a DMF concentration over 40 mol % in Zn-FZS. As shown in fig. S34, this DMF-enriched ZIB provided similar capacity as Zn-MFZS–based solid ZIB in the initial cycles at 2 C but subsequently showed a rapid decay to failure after ~400 cycles. Obviously, DMF itself cannot tolerate persistent volume variation in solid-solid interface, and the superior cycling performance of Zn-MFZS–based ZIB is mainly due to the mesoporous structure of the solid electrolyte, which effectively accommodates volume change and alleviates structural strain/stress during electrochemical reaction (*42*, *43*).

We also evaluated the cycling performance of solid ZIBs with different fluorine-doping concentrations. As shown in fig. S35, Zn-MFZS–based solid ZIB with 5.6 at % of fluorine exhibits a stable cycling over 1000 cycles at 1 C with a capacity retention of 93.2%, which is much better than that of the solid ZIB with 3.9 and 6.2 at % of fluorine Zn-MFZS (40.8 and 61.8% after 1000 cycles, respectively). Optimal fluorine-doping plays an important role in achieving a high ionic conductivity, which greatly affects the electrochemical performance in solid batteries.

Lately, ZIC has received great attention because of its high theoretical gravimetric capacities (820 mA·hour g^{-1}), low cost, and environmental friendliness (*44*, *45*). Furthermore, the low redox potential of Zn anode (−0.76 V, versus standard hydrogen electrode) can extend the voltage window of the capacitor, leading to a high energy and power density (*46*). Nevertheless, the practical application of ZIC has been quite challenging because of the Zn dendrite formation and gas evolution of aqueous electrolyte (*47*). In this work, we successfully fabricated a solid ZIC to fundamentally resolve these issues. By embedding nickel catalysts inside the mesopores, we in situ grew nitrogen-doped few-layer carbon (NDFLC) on MFZS (Fig. 4G) via a typical chemical vapor deposition (CVD) process. By adjusting the concentrations of carbon and nitrogen source, we found that nitrogen doping on few layer carbon also plays a key role on the ionic conductivities of the integrated electrode material after Zn^{2+} insertion (NDFLC@Zn-MFZS; samples S1 to S10 and table S7). Using NDFLC@Zn-MFZS (sample S5; with a carbon and nitrogen content of 17.5 wt % and 9.2 at %, respectively) as positive electrode, Zn-MFZS as solid electrolyte, and Zn foil as negative electrode, the assembled solid ZIC can operate in

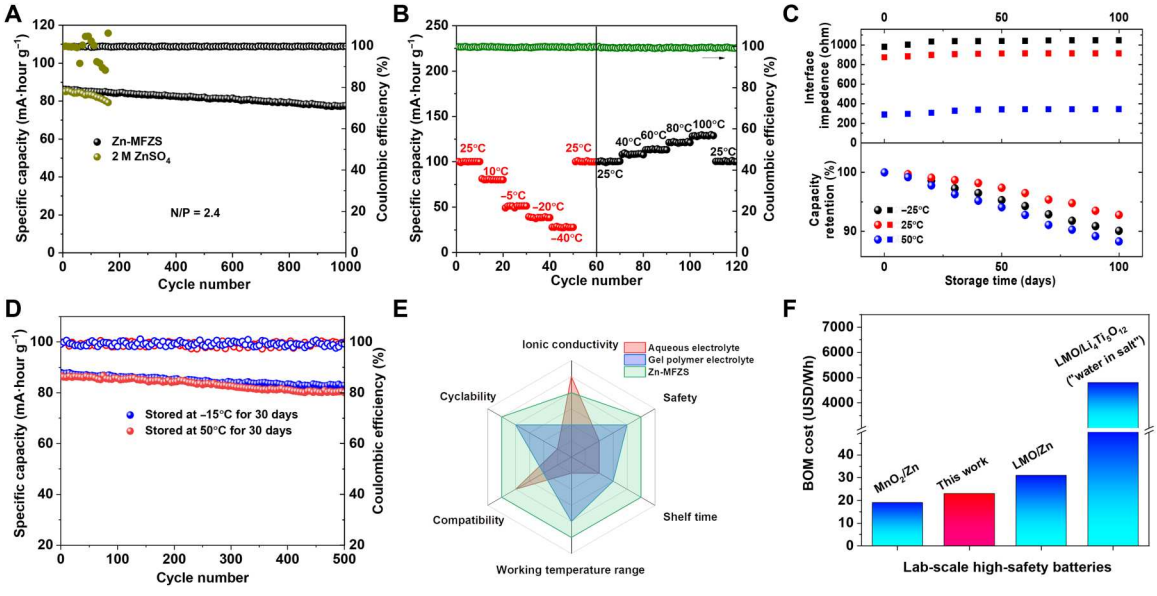

Fig. 5. Electrochemical performance of industrial-level solid ZIBs with itemized evaluations. (**A**) Cycling stability of ZIBs with Zn-MFZS and aqueous $ZnSO_4$ electrolyte under practical conditions (N/P ratio of 2.4) at 2 C. (**B**) Discharge capacity (at 1.5 C) and Coulombic efficiency of solid ZIB with Zn-MFZS under practical conditions at various temperatures. (**C**) Interface impedance and capacity retention of solid ZIB with Zn-MFZS under practical conditions after being stored for 100 days under various temperatures. (**D**) Cycling stability of solid ZIB with Zn-MFZS under practical conditions after being stored for 30 days under various temperatures at 2 C. (**E**) The spider chart for the itemized comparison of Zn-MFZS with other electrolytes for Zn^{2+} energy storage. (**F**) Bill of material (BOM) cost of solid ZIB in this work and other high-safety aqueous lithium and zinc batteries, including $LiMn_2O_4$ (LMO)/Zn (1 M $ZnSO_4$ and 1 M $LiSO_4$ aqueous electrolyte), MnO_2/Zn (2 M $ZnSO_4$ aqueous electrolyte), and LMO/$Li_4Ti_5O_{12}$ (21 M LiTFSI aqueous electrolyte). Materials cost information about these laboratory-scale batteries was mainly taken from https://www.sigmaaldrich.com (one of the major reagent suppliers in the world) on 26 June 2022 (*86*).

a voltage window between 0 and 3 V (Fig. 4H). This solid ZIC showed a high specific capacitance of 133 and 79 mF cm^{-3} at 0.4 and 8 mA cm^{-3}, respectively (see fig. S36 and discussion S4), with a capacitance retention of 94% after 10,000 cycles at 3 mA cm^{-3}. In sharp contrast, ZIC with aqueous $ZnSO_4$ electrolyte quickly short-circuited at 2200th cycle because of dendrite formation (Fig. 4I). Because of the wide operation window of Zn-MFZS, this solid ZIC presents a maximum energy density of 0.04 Wh cm^{-3} at the power density of 0.14 W cm^{-3} and sustains 55% of its energy density at a high power density of 2.79 W cm^{-3}, displaying top-rank energy storage performance among all aqueous or gel polymer–based supercapacitors reported so far (fig. S37) (*48*–*56*). As all the volumetric energy (E_{vol}) and power (P_{vol}) densities from previous literature in fig. S37 are on the basis of the total volume of the device, this performance comparison between solid ZIC and other supercapacitor competitors is valid and fair. These considerable performances of Zn-MFZS–based solid ZIB and ZIC are mainly attributed to the minimized interfacial resistance in integrated electrode-solid electrolyte structure, as well as the dendrite- and hydrogen-free zinc electrode with highly stable Zn^{2+} conductor solid electrolyte.

To evaluate the truly competitive Zn-MFZS–based solid ZIB for industrial applications, we set the negative/positive electrode capacity (N/P) ratio to 2.41 using high MnHCF@Zn-MFZS mass loading (55 mg cm^{-2}, 4.8 mA·hour cm^{-2}) cathode and ultrathin Zn anode (20 μm in thickness, 11.6 mA·hour cm^{-2}). Figure 5A shows the long-term cycling stability of ZIB with Zn-MFZS and aqueous $ZnSO_4$ electrolyte under these testing conductions. Notably, the cycling stability Zn-MFZS–based solid ZIB exhibited nearly 100% Coulombic efficiency and high-capacity retention of 90.7% at 3 C for over 1000 cycles. In comparison, the ZIB with aqueous electrolyte short circuited after only 160 cycles (Fig. 5A), which is due to the fast heterogeneous nucleation of Zn dendrites under these constrained test conditions. We further study the impact of various environmental factors on rate performance of Zn-MFZS–based solid ZIB under practical conditions. As shown in Fig. 5B, this ZIB shows excellent environmental adaptability with a wide working temperature (−40° to 100°C), demonstrating excellent antifreezing and antiheating property. The satisfactory antifreezing and antiheating performance of Zn-MFZS is attributed to the low freezing point and high boiling point of bound DMF molecules, which can serve as the intermediate to complex with Zn^{2+} and promote the migration of Zn^{2+} in a wide temperature range from −70° to 150°C (*57*, *58*). The remarkable capacity up to 129 mA·hour g^{-1} at 100°C is also due to the enhanced ion transport kinetics of Zn-MFZS at high temperature. Similar environmental adaptability was also demonstrated in a polymer solid electrolyte mixed with the same $Zn(OTF)_2$ salt (*59*).

We placed this solid ZIB in various temperature environments to evaluate its shelf life. This solid battery presents a stable interface impedance and negligible capacity loss after 100 days storage at −15°, 25°, and 50°C (Fig. 5C). After being stored at −15° and 50°C, the battery still shows stale cycling with high Coulombic efficiency (Fig. 5D), further revealing a highly reliable feature. Zn-MFZS realizes high stability of solid ZIB with practical battery conditions, which indicates a notable promise for the industrial fabrication in high-capacity solid ZIB. Figure 5E compares Zn-MFZS with frequently reported aqueous and gel polymer electrolyte for ZIBs, using six most important parameters: ionic conductivity, safety, shelf life, working temperature range, compatibility, and cyclability. Zn-MFZS delivers an ultrahigh ionic conductivity and maintains superior safety, shelf life, and cyclability that is absent in typical aqueous and gel polymer electrolyte. In addition, the superiority in terms of compatibility and wide working temperature range makes Zn-MFZS possible to be adapted for different energy storage systems, with simultaneous gains under extremely climate conditions. Last, we estimate the cost of this laboratory-scale solid ZIB based on current market prices for materials, which shows a bill of materials (BOM; including MnHCF@Zn-MFZS cathode, Zn anode, and Zn-MFZS electrolyte) cost of \$23 Wh^{-1} (Fig. 5F). The BOM of this solid ZIB is close to other laboratory-scale high-safety aqueous lithium and zinc batteries (Fig. 5F), such as $LiMn_2O_4$ (LMO)/Zn (\$31 Wh^{-1}) and MnO_2/Zn (\$19 Wh^{-1}), and only 0.48% to the frequently reported high-voltage aqueous lithium battery (LMO/$Li_4Ti_5O_{12}$, \$4800 Wh^{-1}) with concentrated lithium TFSI aqueous electrolyte ("water in salt"; Fig. 5F) (*60*).

DISCUSSION

In this contribution, we have designed a zinc chalcogenide electrolyte for solid-state Zn^{2+} energy storage, with an extremely high ionic conductivity (0.66 mS cm^{-1}) and high Zn^{2+} transference number (0.76) at 25°C. The Zn^{2+} transport in this solid electrolyte follows a rapid ion-hoping mechanism inside the bulk crystals of fluorine-doped, Vac_{Zn}-rich MZS, with the assistance of mesopore channels and residue DMF molecules. This Zn-MFZS ion conductor achieved a hydrogen and dendrite-free Zn plating/stripping and delivered a superior electrochemical performance in both solid ZIBs and ZICs with remarkable temperature adaptability, safety, and shelf life. This mesoporous Zn^{2+} conductor can also function as ion-percolation matrix for the formation of solid-state ionic-conducting network, making it feasible in the fabrication of practical batteries. This design strategy introduces a series of inorganic solid Zn^{2+} conductors with high intrinsic ionic conductivity. For instance, we applied fluorine doping to other mesoporous zinc chalcogenide materials, such as ZnTe and ZnSe. By fitting the Nyquist plot through equivalent circuit (fig. S38 and table S8), the obtained Zn^{2+} preinserted mesoporous Zn–fluorine-doped mesoporous ZnSe (MFZSe) (4.2 at % of fluorine) and Zn–fluorine-doped mesoporous ZnTe (MFZTe) (5.1 at % of fluorine) also show a high room-temperature ionic conductivity of 0.32 and 0.17 mS cm^{-1} (figs. S39 and S40), respectively. This material design introduces a breakthrough avenue for the fabrication of various high-performance inorganic solid Zn^{2+} conductors that should have great potential in solid-state batteries, sensors, and synaptic devices.

MATERIALS AND METHODS

Synthesis of MFZS and Zn-MFZS

Zinc acetate dihydrate ($ZnAc_2$) and thioacetamide (TAA) were used as precursors for the fabrication of MZS, while Pluronic F127 (Sigma-Aldrich) and NH_4F were applied as pore-forming agent and fluorine-doping precursor for the MFZS samples, respectively. The sol solution for EISA was prepared by mixing $ZnAc_2$, TAA, F127, NH_4F, deionized (DI) water, and ethanol (EtOH) with 1:1:0.0053:(0.6 to 1.28):18:30 ($ZnAc_2$:TAA:F127:NH_4F:H_2O:EtOH, molar ratio). The sol was stirred for 2 hours at 25°C and coated on glass substrate to form a film. The glass substrate was aged at 25°C

for 3 days under 50% relative humidity and then calcined at 550°C under air for 2 hours. MFZS powders were obtained by scraping the film from substrate, followed by grinding, washing, and drying. Undoped MZS was prepared in the same manner without the adding of NH_4F in the EISA sol.

Zn-MFZS was synthesized by mixing MFZS powders with a zinc salt solution [0.5 M $Zn(OTF)_2$ in DMF; the molar ratio of $Zn(OTF)_2$ to MFZS is set to 1:10], followed by evaporation of DMF through vacuum drying at 80°C to obtain Zn-MFZS. Zn-MZS was prepared via the same process by replacing MFZS with MZS.

Synthesis of FZS particles

FZS particles with different fluorine-doping concentrations were prepared via the hydrothermal method. Typically, $ZnAC_2$, TAA, NH_4F, and H_2O with the molar ratio of 1:1:(0.79 to 1.61):50 was stirred to form a homogeneous solution, which was then transferred into a Teflon-lined stainless-steel autoclave and heated at 160°C for 8 hours. After cooling, the powders were collected, washed several times under sonication, and then dried at 70°C under vacuum at room temperature.

SPS of Zn-MFZS, Zn-MZS, MFZS, and MZS samples

For SPS treatment (using Dr. Sinter SPS-511S, Sumitomo coal mining Co. Ltd.), the corresponding samples were placed into the mold, and precompression was performed. During SPS, a 10-mm-diameter carbon punch was used and 50-MPa pressure was applied. The samples were held for 10 min at 500°C under vacuum with a ramping rate of 50°C min^{-1}.

Synthesis of MnHCF in situ grown in MFZS

MnHCF in situ gown in MFZS was prepared via a typical corecipitation method. Specifically, 2 mmol of $Mn(NO_3)_2$ was mixed with 100 ml of DI water to form solution 1. MFZS powders (0.133 g) mixed with 0.02 M $K_3Fe(CN)_6$ aqueous solutions (100 ml) were used as solution 2. Then, solution 1 was slowly added into solution 2 by a peristaltic pump for 5 hours. The mixture was stirred for 12 hours at 25°C and aged for another 6 hours. The powders were washed and dried at 80°C for 12 hours. Zn^{2+} insertion was achieved by mixing the obtained powders with 0.5 M $Zn(OTF)_2$ solution in DMF ($Zn(OTF)_2$:MFZS = 1:10, mol/mol), followed by evaporation of DMF through vacuum drying at 80°C to obtain MnHCF@Zn-MFZS (20 wt % of Zn-MFZS).

Synthesis of NDFLC in situ grown in MFZS

Nickel-impregnated MFZS (MFZS/Ni) was firstly prepared by mixing 10 ml of Ni $(NO_3)_2$ aqueous solution (0.5 M) in 1 g of MFZS. After drying and calcination under a H_2/Ar (10%) flow at 450°C, a product of fluorine-doped MZS with nickel nanocrystals (MFZS/Ni) was obtained. NDFLC in situ grown in MFZS was synthesized by CVD process. After filling with polyfurfuryl alcohol and dicyandiamide, MFZS/Ni was heated under H_2/Ar (10%) flow to 1000°C. CVD was initiated by introducing CH_4 and NH_3 into the gas flow with Ar:CH_4:H_2:NH_3 = 300:10:20:100 sccm (standard cubic centimeter per minute). After the sample was cooled under hydrogen flow, the obtained powders were mixed with DMF solution of $Zn(OTF)_2$ ($Zn(OTF)_2$:MFZS = 1:10, mol/mol) to obtain NDFLC@Zn-MFZS.

Synthesis of MFZSe and Zn-MFZSe

$ZnAc_2$ (0.01 mol), F127 (0.053 mmol), NH_4F (0.0082 mol), sodium selenite (0.01 mol), and 30 ml of DI water were stirred for 2 hours at 25°C to obtain a white solution. The solution was transferred to a Teflon-lined stainless-steel autoclave with 30 ml of aqueous hydrazine hydrate. The autoclave was heated to 180°C for 2 hours. After cooling, the resulting precipitate was washed with distilled water and calcinated 650°C under air for 2 hours to obtain MFZSe powder with a fluorine concentration of 4.2 at %. Zn^{2+} insertion was achieved by mixing MFZSe with 0.5 M $Zn(OTF)_2$ solution in DMF [$Zn(OTF)_2$:MFZSe = 1:10, mol/mol], followed by evaporation of DMF through vacuum drying at 80°C to obtain Zn-MFZSe.

Synthesis of MFZTe and Zn-MFZTe

$Zn(NO_3)_2$•$6H_2O$ (0.012 mol), Na_2TeO_3 (0.012 mol), F127 (0.0064 mmol), NH_4F (0.0098 mol), and 30 ml of DI water were stirred for 2 hours at room temperature. $NaBH_4$ (0.02 mol) was added to the above mixture and was kept for stirring, followed by being transferred into a Teflon-lined stainless-steel autoclave. The autoclave was heated at 180°C for 24 hours. The resulting precipitate was washed with distilled water and calcinated 650°C under air for 2 hours to obtain MFZTe powder with a fluorine concentration of 4.8 at %. Zn^{2+} insertion was achieved by mixing MFZTe with 0.5 M $Zn(OTF)_2$ solution in DMF [$Zn(OTF)_2$:MFZTe = 1:10, mol/mol], followed by evaporation of DMF through vacuum drying at 80°C to obtain Zn-MFZTe.

Preparation of integrated structured cathode for solid ZIBs

MnHCF@Zn-MFZS, carbon nanotubes, and polyvinylidene fluoride (PVDF) were grounded with a weight ratio of 7:2:1. Then, the mixture was dispersed in *N*-methylpyrrolidone and cast onto a graphite foil, followed by drying at 70°C for 12 hours. The mass loading of MnHCF@Zn-MFZS is ~5 mg.

Preparation of nonintegrated structured cathode for solid ZIBs

MnHCF was firstly mixed with Zn-MFZS in an agate mortar with the same weight percentage of Zn-MFZS (20 wt %) as that in MnHCF@Zn-MFZS to obtain nonintegrated cathode material (MnHCF/Zn-MFZS). The cathode with nonintegrated structure was made by casting MnHCF/Zn-MFZS with super P carbon and PVDF on graphite foil with a weight ratio of 7:2:1, followed by drying at 70°C.

Assembly of solid ZIB

Zn-MFZS solid electrolyte [with 5 wt % of polytetrafluoroethylene (PTFE) binder] was pressed into a 0.25-mm-thick pellet (with a diameter of 12 mm) under a force of 10 metric tons cm^{-2}. This Zn-MFZS solid electrolyte pellet was further pressed onto the cathode as described above under a force of 10 metric tons cm^{-2}. The solid ZIB was made by coupling this two-layered pellet with a Zn foil (0.1 mm in thickness), which acts as anode. Before battery assembling, a small amount of 0.5 M $Zn(OTF)_2$ solution in 1-ethyl-3-methylimidazolium bis(trifluoromethylsulfonyl)imide (EMIMTFSI) ionic liquid was smeared with a tiny brush on both sides of Zn-MFZS pellet, as well as the surface of cathode and anode (30 μl cm^{-2}), which is typical in solid battery testing (*61*). Subsequently, the battery was placed under vacuum for 45 min, and the smeared solution would form a liquid thin layer to accelerate the migration of

Zn^{2+} from solid electrolyte to cathode/anode during battery cycling. For the fabrication of practical solid ZIB with N/P value of 2.41, high mass loading (4.8 mA·hour cm^{-2}) cathode was coupled with an ultrathin Zn anode (20 μm in thickness, 11.6 mA·hour cm^{-2}).

Assembly of solid ZICs

Zn-MFZS solid electrolyte (with 5 wt % of PTFE binder) was pressed into a 0.25-mm-thick pellet (with a diameter of 12 mm) under 10 metric tons cm^{-2} of force. NDFLC@Zn-MFZS was also pressed into a 2.6-mm-thick pellet (with a diameter of 12 mm) under the same pressure as Zn-MFZS. Solid ZIC was fabricated by pressing a piece of NDFLC@Zn-MFZS pellet and Zn foil onto each side of Zn-MFZS pellet in a 12-mm-diameter die with titanium plungers at 3.8 metric tons cm^{-2} for 15 min. Final ZIC device was assembled by pressing one piece of conductive Cu foil on NDFLC@Zn-MFZS pellet and Zn foil under 3.8 metric tons cm^{-2} for 5 min. A solution of 0.5 M $Zn(OTF)_2$ in EMIMTFSI ionic liquid was smeared on both face of Zn-MFZS pellet (40 μl cm^{-2}) before pressing to ensure the migration of Zn^{2+} from solid electrolyte to electrode. This small amount of solution did not compromise the solid nature of assembled ZIC.

Preparation of ZnF_2 on Zn foil

Zn foil (0.1 mm) was firstly cut into rectangles corresponding to the size of the rectangular corundum crucible (2.5 cm by 10 cm). Then, 0.5 g of NH_4F was added in the crucible, and Zn foil was placed on top. This setup was then transferred into a tube furnace and maintained for 2 hours under Ar flow. Then, a calcination process was conducted at 210°C and held at that temperature for 2 hours to obtain ZnF_2 coated on Zn foil.

Preparation of ZrP powders

The ZrP powders were prepared via a conventional precipitation method. Specifically, 10 g of $ZrOCl_2{\cdot}8H_2O$ was refluxed with 100 ml of 3 M H_3PO_4 at 100°C for 24 hours, and then freeze-dried for 8 hours.

Characterizations

TEM was conducted in a JEOL 2011 microscope. XRD was carried out on a Brucker D8 powder X-ray diffractometer. XPS was carried out in a PHI-5000C ESCA system (PerkinElmer) with Mg Kα radiation ($h\nu$ = 1253.6 eV). DSC was acquired with the DSC 200 F3 Maia (NETZSCH, Germany). Each sample was sealed in hermetic stainless steel (SS) sample pans and weighed. A scanning electron microscope was carried out in the Zeiss Ultra 5 SEM-EDS system. Argon isotherms were collected by Quantachrome Autosorb-iQC at 87 K. ^{19}F solid-state MAS NMR experiments were conducted on a 7.0-T Bruker Avance III spectrometer operating (^{19}F Larmor frequency of 282.2 MHz). The 90° pulse length and recycle delay were set to 1.55 μs and 20 s, respectively. GC-MS was conducted on an Agilent 7890 gas chromatograph with Agilent 5975C mass selective detector. H_2 evolution was measured in sealed Zn/Zn symmetric cell by GC.

Electrochemical characterizations

EIS was conducted on a BioLogic electrochemical working station in a frequency range of 1 MHz to 1 Hz. Two Zn/Zn-MFZS/SS cells were used to perform separate anodic [from open-circuit voltage (OCV) to 4.2 V] and cathodic (from OCV to −0.57 V) scans at 0.1 mV s^{-1} to obtain the electrochemical stability window of Zn-MFZS. The cycling performance of MnHCF based ZIBs batteries with Zn-MFZS solid electrolyte and liquid electrolyte was tested using CR2032 coin-type cells on LAND CT2001A battery test system. Electrochemical stripping/plating for Zn/Zn-MFZS/Zn symmetric cells was conducted on a LAND electrochemical testing system. Solid ZIC was tested in a pelletized cell, which was pressurized by a torque (3.0 N·m) to ensure contact. The electronic conductivity of Zn-MFZS was measured by the four-probe methods (Shimadzu, JXA-8230) at different pressures at room temperature. The ion conductivity of various ZnS-based electrolytes was measured by Admiral Instruments electrochemical workstation within the frequency range 100 kHz to 0.1 Hz at different temperatures (25° to 90°C) (*20*, *62*, *63*). The powder sample was firstly pressed to 2.6-mm pellet under 20 metric tons of force. Then, the pellet was sandwiched between two stainless-steel spacers to measure the EIS. Ionic conductivity (σ) was calculated on the basis of the equation of $= l/RS$, where R is the total impedance according to EIS measurement, l is the sample thickness (2.6 mm), and S represents the area (1.13 cm^2).

Supplementary Materials

This PDF file includes:

Discussions S1 to S4
Figs. S1 to S40
Tables S1 to S8

REFERENCES AND NOTES

1. M. S. Whittingham, Special editorial perspective: Beyond Li-ion battery chemistry. *Chem. Rev.* **120**, 6328–6330 (2020).
2. G. Fang, J. Zhou, A. Pan, S. Liang, Recent advances in aqueous zinc-ion batteries. *ACS Energy Lett.* **3**, 2480–2501 (2018).
3. F. Wu, M. Liu, Y. Li, X. Feng, K. Zhang, Y. Bai, X. Wang, C. Wu, High-mass-loading electrodes for advanced secondary batteries and supercapacitors. *Electrochem. Energy Rev.* **4**, 382–446 (2021).
4. X. Yuan, F. Ma, L. Zuo, J. Wang, N. Yu, Y. Chen, Y. Zhu, Q. Huang, R. Holze, Y. Wu, T. van Ree, Latest advances in high-voltage and high-energy-density aqueous rechargeable batteries. *Electrochem. Energy Rev.* **4**, 1–34 (2021).
5. T. Zhang, Y. Tang, S. Guo, X. Cao, A. Pan, G. Fang, J. Zhou, S. Liang, Fundamentals and perspectives in developing zinc-ion battery electrolytes: A comprehensive review. *Energ. Environ. Sci.* **13**, 4625–4665 (2020).
6. D. K. Bharti, M. K. Gupta, A. K. Srivastava, Temperature dependent dielectric and electric properties of zinc silicate nanorods. *Nano-Struct. Nano-Objects* **17**, 123–128 (2019).
7. Y. Wang, W. D. Richards, S. P. Ong, L. J. Miara, J. C. Kim, Y. Mo, G. Ceder, Design principles for solid-state lithium superionic conductors. *Nat. Mater.* **14**, 1026–1031 (2015).
8. S. P. Ong, W. D. Richards, A. Jain, G. Hautier, M. Kocher, S. Cholia, D. Gunter, V. L. Chevrier, K. A. Persson, G. Ceder, Python Materials Genomics (pymatgen): A robust, open-source python library for materials analysis. *Comput. Mater. Sci.* **68**, 314–319 (2013).
9. S. S. Shinde, P. S. Shinde, S. M. Pawar, A. V. Moholkar, C. H. Bhosale, K. Y. Rajpure, Physical properties of transparent and conducting sprayed fluorine doped zinc oxide thin films. *Solid State Sci.* **10**, 1209–1214 (2008).
10. R. Ferro, J. A. Rodriguez, O. Vigil, A. Morales-Acevedo, G. Contreras-Puente, F-doped CdO thin films deposited by spray pyrolysis. *Physica Status Solidi (a)* **177**, 477–483 (2000).
11. E. Elangovan, K. Ramamurthi, A study on low cost-high conducting fluorine and antimony-doped tin oxide thin films. *Appl. Surf. Sci.* **249**, 183–196 (2005).
12. D. Liu, J. Zhou, J. Wang, R. Tian, X. Li, E. Nie, X. Piao, Z. Sun, Enhanced visible light photoelectrocatalytic degradation of organic contaminants by F and Sn co-doped TiO_2 photoelectrode. *Chem. Eng. J.* **344**, 332–341 (2018).
13. J. Chen, Z. Yu, P. Zhu, J. Wang, Z. Gan, J. Wei, Y. Zhao, S. Wei, Effects of fluorine on the structure of fluorohydroxyapatite: A study by XRD, solid-state NMR and Raman spectroscopy. *J. Mater. Chem. B* **3**, 34–38 (2015).
14. A. R. Denton, N. W. Ashcroft, Vegard's law. *Phys. Rev. A* **43**, 3161–3164 (1991).

15. C. Yang, Q. Wu, W. Xie, X. Zhang, A. Brozena, J. Zheng, M. N. Garaga, B. H. Ko, Y. Mao, S. He, Y. Gao, P. Wang, M. Tyagi, F. Jiao, R. Briber, P. Albertus, C. Wang, S. Greenbaum, Y. Y. Hu, A. Isogai, M. Winter, K. Xu, Y. Qi, L. Hu, Copper-coordinated cellulose ion conductors for solid-state batteries. *Nature* **598**, 590–596 (2021).
16. W. Guo, J. Chen, S. Sun, Q. Zhou, In situ monitoring the molecular diffusion process in graphene oxide membranes by ATR-FTIR spectroscopy. *J. Phys. Chem. C* **120**, 7451–7456 (2016).
17. M. Trejda, M. Ziolek, P. Decyk, D. Duczmal, The radical species and impurities present in mesoporous silicas as oxidation active centres. *Microporous Mesoporous Mater.* **120**, 214–220 (2009).
18. K. M. Abraham, Z. Jiang, B. Carroll, Highly conductive PEO-like polymer electrolytes. *Chem. Mater.* **9**, 1978–1988 (1997).
19. P. G. Bruce, J. Evans, C. A. Vincent, Conductivity and transference number measurements on polymer electrolytes. *Solid State Ion.* **28**, 918–922 (1988).
20. Z. Wang, J. Hu, L. Han, Z. Wang, H. Wang, Q. Zhao, J. Liu, F. Pan, A MOF-based single-ion Zn^{2+} solid electrolyte leading to dendrite-free rechargeable Zn batteries. *Nano Energy* **56**, 92–99 (2019).
21. K. Fujie, K. Otsubo, R. Ikeda, T. Yamada, H. Kitagawa, Low temperature ionic conductor: Ionic liquid incorporated within a metal–organic framework. *Chem. Sci.* **6**, 4306–4310 (2015).
22. P. Kurek, M. W. Breiter, Thermal stability and ionic conductivity of the BIMEVOX. 10 ceramics (ME = Zn, Ni). *Solid State Ionics* **86**, 131–135 (1996).
23. L. C. De Jonghe, L. Feldman, A. Beuchele, Slow degradation and electron conduction in sodium/beta-aluminas. *J. Mater. Sci.* **16**, 780–786 (1981).
24. L. C. De Jonghe, Transport number gradients and solid electrolyte degradation. *J. Electrochem. Soc.* **129**, 752–755 (1982).
25. I. T. Todorov, W. Smith, K. Trachenko, M. T. Dove, DL_POLY_3: New dimensions in molecular dynamics simulations via massive parallelism. *J. Mater. Chem.* **16**, 1911–1918 (2006).
26. A. J. Zapata, Y. Gu, G. B. Hammond, The first α-fluoroallenylphosphonate, the synthesis of conjugated fluoroenynes, and the stereoselective synthesis of Vinylfluorophosphonates using a new multifunctional fluorine-containing building block. *J. Org. Chem.* **65**, 227–234 (2000).
27. Y. Yoshida, T. Yamada, Y. Jing, T. Toyao, K. I. Shimizu, M. Sadakiyo, Super Mg^{2+} conductivity around 10^{-3} S cm^{-1} Observed in a porous metal–organic framework. *J. Am. Chem. Soc.* **144**, 8669–8675 (2022).
28. J. Chen, C. Lin, D. Zhao, M. Luo, G. Peng, B. Li, S. Yang, Y. Sun, N. Ye, Anionic aliovalent substitution from structure models of ZnS: Novel defect diamond-like halopnictide infrared nonlinear optical materials with wide band gaps and large SHG effects. *Angew. Chem. Int. Ed.* **59**, 23549–23553 (2020).
29. J. C. Dyre, P. Maass, B. Roling, D. L. Sidebottom, Fundamental questions relating to ion conduction in disordered solids. *Rep. Prog. Phys.* **72**, 046501 (2009).
30. T. Heitmann, G. Hester, S. Mitra, T. Calloway, M. S. Tyagi, A. Miskowiec, S. Diallo, N. Osti, E. Mamontov, Probing Li ion dynamics in amorphous $xLi_2SO_4{\cdot}(1-x)\ LiPO_3$ by quasielastic neutron scattering. *Solid State Ion.* **334**, 95–98 (2019).
31. A. Bayaguud, Y. Fu, C. Zhu, Interfacial parasitic reactions of zinc anodes in zinc ion batteries: Underestimated corrosion and hydrogen evolution reactions and their suppression strategies. *Journal of Energy Chemistry* **64**, 246–262 (2022).
32. C. Deng, X. Xie, J. Han, Y. Tang, J. Gao, C. Liu, X. Shi, J. Zhou, S. Liang, A sieve-functional and uniform-porous kaolin layer toward stable zinc metal anode. *Adv. Funct. Mater.* **30**, 2000599 (2020).
33. K. Chen, H. Guo, W. Li, Y. Wang, Dual porous 3D zinc anodes toward dendrite-free and long cycle life zinc-ion batteries. *ACS Appl. Mater. Interfaces* **13**, 54990–54996 (2021).
34. H. Chen, Y. Rong, Z. Yang, L. Deng, J. Wu, V_2O_3@amorphous carbon as a cathode of zinc ion batteries with high stability and long cycling life. *Ind. Eng. Chem. Res.* **60**, 1517–1525 (2021).
35. F. Long, Y. Xiang, S. Yang, Y. Li, H. du, Y. Liu, X. Wu, X. Wu, Layered manganese dioxide nanoflowers with Cu^{2+} and Bi^{3+} intercalation as high-performance cathode for aqueous zinc-ion battery. *J. Colloid Interface Sci.* **616**, 101–109 (2022).
36. A. Chen, C. Zhao, Z. Guo, X. Lu, N. Liu, Y. Zhang, L. Fan, N. Zhang, Fast-growing multifunctional $ZnMoO_4$ protection layer enable dendrite-free and hydrogen-suppressed Zn anode. *Energy Storage Mater.* **44**, 353–359 (2022).
37. Y. Qin, P. Liu, Q. Zhang, Q. Wang, D. Sun, Y. Tang, Y. Ren, H. Wang, Advanced filter membrane separator for aqueous zinc-ion batteries. *Small* **16**, 2003106 (2020).
38. P. Xiao, H. Li, J. Fu, C. Zeng, Y. Zhao, T. Zhai, H. Li, An anticorrosive zinc metal anode with ultra-long cycle life over one year. *Energ. Environ. Sci.* **15**, 1638–1646 (2022).
39. R. Zhao, H. Wang, H. Du, Y. Yang, Z. Gao, L. Qie, Y. Huang, Lanthanum nitrate as aqueous electrolyte additive for favourable zinc metal electrodeposition. *Nat. Commun.* **13**, 1–9 (2022).
40. S. Li, Y. Liu, X. Zhao, Q. Shen, W. Zhao, Q. Tan, N. Zhang, P. Li, L. Jiao, X. Qu, Sandwich-like heterostructures of MoS_2/graphene with enlarged interlayer spacing and enhanced hydrophilicity as high-performance cathodes for aqueous zinc-ion batteries. *Adv. Mater.* **33**, 2007480 (2021).
41. C. Liu, Z. Li, X. Zhang, W. Xu, W. Chen, K. Zhao, Y. Wang, S. Hong, Q. Wu, M.-C. Li, C. Mei, Synergic effect of dendrite-free and zinc gating in lignin-containing cellulose nanofibers-MXene layer enabling long-cycle-life zinc metal batteries. *Adv. Sci.* **9**, 2202380 (2022).
42. Y. Xu, G. Jian, Y. Liu, Y. Zhu, M. R. Zachariah, C. Wang, Superior electrochemical performance and structure evolution of mesoporous Fe_2O_3 anodes for lithium-ion batteries. *Nano Energy* **3**, 26–35 (2014).
43. W. Li, J. Liu, D. Zhao, Mesoporous materials for energy conversion and storage devices. *Nat. Rev. Mater.* **1**, 1–17 (2016).
44. L. Han, H. Huang, X. Fu, J. Li, Z. Yang, X. Liu, L. Pan, M. Xu, A flexible, high-voltage and safe zwitterionic natural polymer hydrogel electrolyte for high-energy-density zinc-ion hybrid supercapacitor. *Chem. Eng. J.* **392**, 123733 (2020).
45. Z. Li, Y. An, S. Dong, C. Chen, L. Wu, Y. Sun, X. Zhang, Progress on zinc ion hybrid supercapacitors: Insights and challenges. *Energy Storage Mater.* **31**, 252–266 (2020).
46. H. Wang, W. Ye, Y. Yang, Y. Zhong, Y. Hu, Zn-ion hybrid supercapacitors: Achievements, challenges and future perspectives. *Nano Energy* **85**, 105942 (2021).
47. X. Gong, J. Chen, P. S. Lee, Zinc-ion hybrid supercapacitors: Progress and future perspective. *Batter. Supercaps* **4**, 1529–1546 (2021).
48. L. Kou, T. Huang, B. Zheng, Y. Han, X. Zhao, K. Gopalsamy, H. Sun, C. Gao, Coaxial wet-spun yarn supercapacitors for high-energy density and safe wearable electronics. *Nat. Commun.* **5**, 1–10 (2014).
49. Y. Huang, H. Hu, Y. Huang, M. Zhu, W. Meng, C. Liu, Z. Pei, C. Hao, Z. Wang, C. Zhi, From industrially weavable and knittable highly conductive yarns to large wearable energy storage textiles. *ACS Nano* **9**, 4766–4775 (2015).
50. S. Padmajan Sasikala, K. E. Lee, J. Lim, H. J. Lee, S. H. Koo, I. H. Kim, H. J. Jung, S. O. Kim, Interface-confined high crystalline growth of semiconducting polymers at graphene fibers for high-performance wearable supercapacitors. *ACS Nano* **11**, 9424–9434 (2017).
51. H. Wang, M. Wang, Y. Tang, A novel zinc-ion hybrid supercapacitor for long-life and low-cost energy storage applications. *Energy Storage Mater.* **13**, 1–7 (2018).
52. J. Zhang, X. Zhao, Z. Huang, T. Xu, Q. Zhang, High-performance all-solid-state flexible supercapacitors based on manganese dioxide/carbon fibers. *Carbon* **107**, 844–851 (2016).
53. Z. Zhang, F. Xiao, S. Wang, Hierarchically structured MnO_2/graphene/carbon fiber and porous graphene hydrogel wrapped copper wire for fiber-based flexible all-solid-state asymmetric supercapacitors. *J. Mater. Chem. A* **3**, 11215–11223 (2015).
54. Y. Hu, H. Cheng, F. Zhao, N. Chen, L. Jiang, Z. Feng, L. Qu, All-in-one graphene fiber supercapacitor. *Nanoscale* **6**, 6448–6451 (2014).
55. L. Hua, Z. Ma, P. Shi, L. Li, K. Rui, J. Zhou, X. Huang, X. Liu, J. Zhu, G. Sun, W. Huang, Ultrathin and large-sized vanadium oxide nanosheets mildly prepared at room temperature for high performance fiber-based supercapacitors. *J. Mater. Chem. A* **5**, 2483–2487 (2017).
56. S. Zhai, H. E. Karahan, L. Wei, X. Chen, Z. Zhou, X. Wang, Y. Chen, Hydrothermal assembly of micro-nano-integrated core-sheath carbon fibers for high-performance all-carbon microsupercapacitors. *Energy Storage Mater.* **9**, 221–228 (2017).
57. N. Wang, X. Dong, B. Wang, Z. Guo, Z. Wang, R. Wang, X. Qiu, Y. Wang, Zinc–organic battery with a wide operation-temperature window from −70 to 150°C. *Angew. Chem. Int. Ed.* **59**, 14577–14583 (2020).
58. Z. Liu, X. Luo, L. Qin, G. Fang, S. Liang, Progress and prospect of low-temperature zinc metal batteries. *Advanced Powder Materials* **1**, 100011 (2022).
59. Z. Chen, X. Li, D. Wang, Q. Yang, L. Ma, Z. Huang, G. Liang, A. Chen, Y. Guo, B. Dong, X. Huang, C. Yang, C. Zhi, Grafted MXene/polymer electrolyte for high performance solid zinc batteries with enhanced shelf life at low/high temperatures. *Energ. Environ. Sci.* **14**, 3492–3501 (2021).
60. J. Chen, J. Vatamanu, L. Xing, O. Borodin, H. Chen, X. Guan, X. Liu, K. Xu, W. Li, Improving electrochemical stability and low-temperature performance with water/acetonitrile hybrid electrolytes. *Advanced Energy Mater.* **10**, 1902654 (2020).
61. X. Chi, M. Li, J. di, P. Bai, L. Song, X. Wang, F. Li, S. Liang, J. Xu, J. Yu, A highly stable and flexible zeolite electrolyte solid-state Li–air battery. *Nature* **592**, 551–557 (2021).
62. X. Zeng, J. Mao, J. Hao, J. Liu, S. Liu, Z. Wang, Y. Wang, S. Zhang, T. Zheng, J. Liu, P. Rao, Z. Guo, Electrolyte design for in situ construction of highly Zn^{2+}–conductive solid electrolyte interphase to enable high-performance aqueous Zn-ion batteries under practical conditions. *Adv. Mater.* **33**, 2007416 (2021).
63. W. Xin, L. Miao, L. Zhang, H. Peng, Z. Yan, Z. Zhu, Turning the byproduct $Zn_4(OH)_6SO_4{\cdot}xH_2O$ into a uniform solid electrolyte interphase to stabilize aqueous Zn anode. *ACS Materials Lett.* **3**, 1819–1825 (2021).
64. J. Hao, B. Li, X. Li, X. Zeng, S. Zhang, F. Yang, S. Liu, D. Li, C. Wu, Z. Guo, An in-depth study of Zn metal surface chemistry for advanced aqueous Zn-ion batteries. *Adv. Mater.* **32**, 2003021 (2020).

65. J. Han, H. Euchner, M. Kuenzel, S. M. Hosseini, A. Groß, A. Varzi, S. Passerini, A thin and uniform fluoride-based artificial interphase for the zinc metal anode enabling reversible Zn/MnO_2 batteries. *ACS Energy Letters* **6**, 3063–3071 (2021).
66. J. Yan, M. Ye, Y. Zhang, Y. Tang, C. C. Li, Layered zirconium phosphate-based artificial solid electrolyte interface with zinc ion channels towards dendrite-free Zn metal anodes. *Chem. Eng. J.* **432**, 134227 (2022).
67. M. He, C. Shu, A. Hu, R. Zheng, M. Li, Z. Ran, J. Long, Suppressing dendrite growth and side reactions on Zn metal anode via guiding interfacial anion/cation/H_2O distribution by artificial multi-functional interface layer. *Energy Storage Mater.* **44**, 452–460 (2021).
68. X. Han, Y. Gong, K. Fu, X. He, G. T. Hitz, J. Dai, A. Pearse, B. Liu, H. Wang, G. Rubloff, Y. Mo, V. Thangadurai, E. D. Wachsman, L. Hu, Negating interfacial impedance in garnet-based solid-state Li metal batteries. *Nat. Mater.* **16**, 572–579 (2017).
69. A. Sharafi, E. Kazyak, A. L. Davis, S. Yu, T. Thompson, D. J. Siegel, N. P. Dasgupta, J. Sakamoto, Surface chemistry mechanism of ultra-low interfacial resistance in the solid-state electrolyte $Li_7La_3Zr_2O_{12}$. *Chem. Mater.* **29**, 7961–7968 (2017).
70. F. Han, J. Yue, X. Zhu, C. Wang, Suppressing Li dendrite formation in Li_2S-P_2S_5 Solid electrolyte by LiI incorporation. *Advanced Energy Materials* **8**, 1703644 (2018).
71. E. Rangasamy, Z. Liu, M. Gobet, K. Pilar, G. Sahu, W. Zhou, H. Wu, S. Greenbaum, C. Liang, An iodide-based $Li_7P_2S_8I$ superionic conductor. *J. Am. Chem. Soc.* **137**, 1384–1387 (2015).
72. J. Zhao, K. K. Sonigara, J. Li, J. Zhang, B. Chen, J. Zhang, S. S. Soni, X. Zhou, G. Cui, L. Chen, A smart flexible zinc battery with cooling recovery ability. *Angew. Chem. Int. Ed.* **56**, 7871–7875 (2017).
73. Z. Liu, D. Wang, Z. Tang, G. Liang, Q. Yang, H. Li, L. Ma, F. Mo, C. Zhi, A mechanically durable and device-level tough Zn-MnO_2 battery with high flexibility. *Energy Storage Mater.* **23**, 636–645 (2019).
74. S. Huang, F. Wan, S. Bi, J. Zhu, Z. Niu, J. Chen, A self-healing integrated all-in-one zinc-ion battery. *Angew. Chem. Int. Ed.* **58**, 4313–4317 (2019).
75. Q. Han, X. Chi, S. Zhang, Y. Liu, B. Zhou, J. Yang, Y. Liu, Durable, flexible self-standing hydrogel electrolytes enabling high-safety rechargeable solid-state zinc metal batteries. *J. Mater. Chem. A* **6**, 23046–23054 (2018).
76. J. Huang, X. Chi, Q. Han, Y. Liu, Y. du, J. Yang, Y. Liu, Thickening and homogenizing aqueous electrolyte towards highly efficient and stable Zn metal batteries. *J. Electrochem. Soc.* **166**, A1211–A1216 (2019).
77. K. Zhao, C. Wang, Y. Yu, M. Yan, Q. Wei, P. He, Y. Dong, Z. Zhang, X. Wang, L. Mai, Ultrathin surface coating enables stabilized zinc metal anode. *Adv. Mater. Interfaces* **5**, 1800848 (2018).
78. Y. Zeng, X. Zhang, Y. Meng, M. Yu, J. Yi, Y. Wu, X. Lu, Y. Tong, Achieving ultrahigh energy density and long durability in a flexible rechargeable quasi-solid-state Zn-MnO_2 Battery. *Adv. Mater.* **29**, 1700274 (2017).
79. J. Sun, Y. Zhang, Y. Liu, H. Jiang, X. Dong, T. Hu, C. Meng, Hydrated vanadium pentoxide/reduced graphene oxide-polyvinyl alcohol ($V_2O_5 \cdot nH_2O$/rGO-PVA) film as a binder-free electrode for solid-state Zn-ion batteries. *J. Colloid Interface Sci.* **587**, 845–854 (2021).
80. Y. Huang, J. Zhang, J. Liu, Z. Li, S. Jin, Z. Li, S. Zhang, H. Zhou, Flexible and stable quasi-solid-state zinc ion battery with conductive guar gum electrolyte. *Materials Today Energy* **14**, 100349 (2019).
81. A. Huang, J. Chen, W. Zhou, A. Wang, M. Chen, Q. Tian, J. Xu, Electrodeposition of MnO_2 nanoflakes onto carbon nanotube film towards high-performance flexible quasi-solid-state Zn-MnO_2 batteries. *J. Electroanal. Chem.* **873**, 114392 (2020).
82. F. Guo, S. Gao, C. Ji, H. Mi, H. Li, W. Zhang, H. Pang, Finely crafted polyaniline cathode for high-performance flexible quasi-solid-state Zn-ion battery. *Solid State Ion.* **364**, 115612 (2021).
83. Y. Ma, X. Xie, R. Lv, B. Na, J. Ouyang, H. Liu, Nanostructured polyaniline–cellulose papers for solid-state flexible aqueous Zn-ion battery. *ACS Sustainable Chemistry & Engineering* **6**, 8697–8703 (2018).
84. D. Chao, C. R. Zhu, M. Song, P. Liang, X. Zhang, N. H. Tiep, H. Zhao, J. Wang, R. Wang, H. Zhang, H. J. Fan, A high-rate and stable quasi-solid-state zinc-ion battery with novel 2D layered zinc orthovanadate array. *Adv. Mater.* **30**, 1803181 (2018).
85. Z. Pan, J. Yang, J. Yang, Q. Zhang, H. Zhang, X. Li, Z. Kou, Y. Zhang, H. Chen, C. Yan, J. Wang, Stitching of $Zn_3(OH)_2V_2O_7 \cdot 2H_2O$ 2D nanosheets by 1D carbon nanotubes boosts ultrahigh rate for wearable quasi-solid-state zinc-ion batteries. *ACS Nano* **14**, 842–853 (2020).
86. Merck, 2002; www.sigmaaldrich.com.

Acknowledgments: We thank C. Pu from the Department of Chemical Engineering in University of Waterloo for the support of battery testing and sample preparation. We also thank M. Han and Z. Liu from the Department of Chemical Engineering in University of Waterloo for the assistance in XRD and SEM characterizations. **Funding:** This study has been possible thanks to financial support from the National Natural Science Foundation of China (grant no. 21871008) and Shanghai Science and Technology Innovation Action Plan (20dz1204400). The theoretical calculation was supported by High-Performance Computing Platform of Peking University. **Author contributions:** Conception and design of the study: J.Z. and F.H. Acquisition and analysis of the data: J.Z., S.Z., and M.Z. Manuscript drafting and figure preparation: J.Z., S.Z., and R.W. **Competing interests:** The authors declare that they have no competing interests. **Data and materials availability:** All data needed to evaluate the conclusions in the paper are present in the paper and/or the Supplementary Materials.

Submitted 1 August 2022
Accepted 30 December 2022
Published 27 January 2023
10.1126/sciadv.ade2217